Journal of Materials Chemistry C

Effect of annealing conditions on the electrical properties of ALD-grown polycrystalline BiFeO3 films

Journal:	*Journal of Materials Chemistry C*
Manuscript ID	TC-ART-12-2017-005755.R1
Article Type:	Paper
Date Submitted by the Author:	24-Mar-2018
Complete List of Authors:	Golovina, Iryna; Drexel University, Materials Science + Engineering Falmbigl, Matthias; Drexel University, Materials Science + Engineering Plokhikh, Aleksandr; Drexel University, Materials Science + Engineering Parker, Thomas; US Army Research Laboratory Johnson, Craig; Drexel Univ, Spanier, Jonathan; Drexel University, Materials Science + Engineering

Effect of annealing conditions on the electrical properties of ALD-grown polycrystalline $BiFeO_3$ films

Iryna S. Golovina[1,2], Matthias Falmbigl[1], Aleksandr V. Plokhikh[1], Thomas C. Parker[3], Craig Johnson[1] and Jonathan E. Spanier[1,4,5*]

[1]*Department of Materials Science & Engineering, Drexel University, Philadelphia, Pennsylvania 19104, USA*

[2]*Institute of Semiconductor Physics, National Academy of Sciences of Ukraine, Kyiv 03028, Ukraine*

[3]*US Army Research Laboratory, Aberdeen Proving Ground, Maryland 21005, USA*

[4]*Department of Electrical & Computer Engineering, Drexel University, Philadelphia, Pennsylvania 19104, USA*

[5]*Department of Physics, Drexel University, Philadelphia, Pennsylvania 19104, USA*

[*]Corresponding Author

Address: Drexel University, Materials Science & Engineering Department

3141 Chestnut Street, Philadelphia, PA 19104, USA

Email: spanier@drexel.edu

Phone: (215)895-2301

Abstract

An investigation of the influence of annealing conditions on the carrier transport, leakage current and dielectric properties of ALD-grown amorphous Bi-Fe-O thin films after their crystallization into $BiFeO_3$ is presented. Whereas the interface-limited Schottky emission mechanism is dominant in 70 nm thick Fe-rich films after relatively short annealing, a space-charge-limited conduction mechanism is dominant in stoichiometric films with a thickness of 215 nm independent of the annealing conditions. Interestingly, prolonged annealing of the thin films also results in space charge limited conduction. Analysis of the changes in dielectric properties, on one hand, and the film composition, microstructure and morphology, on the other hand, reveal the key role of grain boundary interfaces for the conductivity of the polycrystalline ALD-grown $BiFeO_3$ thin films. Extended annealing in oxygen results in 2-3 orders-of-magnitude reduction in leakage current accompanied by decreases in dielectric loss, highlighting the importance of optimizing annealing conditions for any applications of $BiFeO_3$ thin films.

Introduction

Bismuth ferrite, $BiFeO_3$ (BFO) has proven to be promising for a wide variety of microelectronic devices and photovoltaic applications.[1-8] Being a room-temperature multiferroic, BFO films can be used in ferroelectric memory devices, magnetoelectric and spintronic applications.[1,2] Mixing with other compounds, *e.g.*, with $PbTiO_3$ and $SmFeO_3$ and thereby forming a morphotropic phase boundary (MPB), produces large piezoelectric coefficients.[3,4] After exposure to femtosecond laser pulses, BFO films emit terahertz radiation, which is attractive for applications in the telecommunication and security sectors.[5,6] However, a wide usage of BFO films for almost every kind of application is limited by the large leakage current. As numerous studies unraveled, the main sources of conductivity are oxygen vacancies and Fe^{2+} ions being formed during the fabrication process[7-10], as well as contributions from parasitic phases, such as Bi_2O_3.[11] Previously, several approaches where attempted to decrease the leakage current in BFO. One way is *A*-site substitution for the Bi^{3+} ion and/or *B*-site substitution for the Fe^{3+} ion in the ABO_3 perovskite structure. For example, the BFO samples were doped with La,[12] Dy,[12] Sm,[4] Ho,[13,14] Nd,[15] Gd,[16,17] Lu,[18] or co-doped with Gd and Ti.[19] Some doped samples exhibit a reduced leakage current and along with that demonstrate improved characteristics, *e.g.*, increased piezoelectric constant for Sm-[4] and Nd-doped[20] samples or enhanced magnetization for the Ho-,[14] Nd-[15] and Lu-doped samples.[18] However, doping may sometimes introduce impurity phases and can induce structural phase transitions.[21] An alternative route for improving the material functionality is modifying the synthesis conditions. In this respect, the effects of the growth temperature, oxygen pressure,[22,23] repetition rate,[24] and nonstoichiometry[25] on the microstructure and ferroelectric properties of BFO films grown by pulsed laser deposition (PLD) were studied. The influence of the sputtering gas pressure and heat-treatment temperature on the electrical and magnetic properties of radio-frequency (RF) magnetron sputtered BFO films was investigated.[26,27] Furthermore, the effects of annealing atmospheres such as air, N_2 and O_2[28]

and annealing temperature[29] on the structural and the electrical properties of BFO thin films obtained by chemical solution deposition techniques were studied. Finally, contact phenomena, *i.e*. electrode-film interface, have a strong influence on the functional characteristics of thin films.[30,31]

Atomic layer deposition (ALD) and post-growth annealing is an appealing route for attaining BFO thin films at reduced deposition temperatures compared with physical vapor deposition methods, *e.g*., PLD and RF sputtering, or metal-organic chemical vapor deposition (MOCVD). Moreover, ALD permits a unique upscaling capability due to precise thickness control and high conformity of the growth process.[32-34] Since the first reports of synthesis of BFO films utilizing ALD in 2013,[35,36] several studies on the microstructure and properties of ALD-grown BFO films were conducted.[37-42] While BFO can be grown epitaxial or polycrystalline depending on the choice of substrate, in all cases the as-grown films appear amorphous and post-processing by heat treatment is mandatory regardless of the epitaxial or polycrystalline nature of the films. Until now, information on the influence of these annealing conditions on the resulting properties of ALD-grown BFO films is absent, to the best of our knowledge. In particular, a detailed understanding of the interplay between annealing conditions and conduction mechanisms is vital for any applications of ALD-grown BFO thin films.

Herein, we apply different annealing procedures to two sets of films, one of them a stoichiometric film with a thickness of 215 nm and the other one a Fe-rich (or Bi-deficient) film with a thickness of 70 nm. The Fe-rich film is the film where incomplete crystallization occurs. Therefore, in this film amorphous FeO_x layers are expected to still be present between crystalline BFO. The influence of Fe_2O_3 impurities on the electrical and ferroelectric properties of BFO was investigated earlier.[41-43] While A. Lahma *et al*.[43] claim that presence of Fe_2O_3 phase increases the conductivity of BFO film, S. Fujino *et al*.[44] show that multiphase $BiFeO_3$ thin films which contain Fe_2O_3 inclusions have lower leakage current than pure BFO film. In latter case, authors mention that since grain boundaries are considered as leakage

paths, the Fe_2O_3 regions play the role of "plugging" up the grain boundaries between BFO grains, thus minimizing the leakage current. M. Puttaswamy *et al*.[42] also note that films with Bi/Fe = 0.6 demonstrate lower current densities in comparison to the films with Bi/Fe = 1.3. To the best of our knowledge, there is no information on the impact of amorphous FeO_x layers on the electrical properties of BFO films grown by ALD method using a superlattice approach. In this regard, FeO_x layers embedded in BFO could be considered as a new type of a nanocomposite material.

In order to correlate the resulting properties to the structure, morphology and composition, films were characterized by X-ray diffraction (XRD), transmission electron microscopy (TEM), atomic force microscopy (AFM), energy dispersive spectroscopy (EDS), Rutherford backscattering spectrometry (RBS) and X-ray photoelectron spectroscopy (XPS) techniques after each annealing process. Whereas the maximum annealing temperature was kept at 550°C in all cases, the annealing atmosphere and heating cycles were altered. In each case the current and voltage relationship was investigated and the dominant conduction mechanism was determined. Our results reveal not only an enhanced contribution of the contact interface to the conductivity for the thinner Fe-rich films, but also for a larger amount of iron and/or oxygen vacancies increases. We demonstrate that the leakage current can be substantially reduced by varying the annealing conditions, and that the dielectric properties, *i.e*. dielectric constant, losses and tunability of the BFO films can be improved significantly.

Experimental

ALD of the two Bi-Fe-O thin films was performed in a Picosun R200 Advanced reactor on Pt(111)/Ti/SiO_2/Si(100) substrates (Gmek Inc.) and Si(100) substrates (Addison Engineering Inc.) having a native oxide layer. High purity nitrogen (99.9999%) gas was used as carrier gas. Ferrocene ($Fe(Cp)_2$, Alfa Aesar, 99% purity) and Bi-triphenyl ($Bi(ph)_3$, Alfa Aesar, 99+% purity) were evaporated

at 180°C and 200°C, respectively. Ozone in a concentration higher than 200 gm^{-3} was produced by an IN-USA generator and introduced into the reaction chamber by a separate line. The deposition temperature was 250 °C. The growth was conducted using the following pulse sequence [($Fe(Cp)_2$-O_3) x *a* + ($Bi(Ph)_3$-O_3) x *b*)] x *c*, with *a*, *b*, *c* = 100, 100, 13 for the 70 nm thick film and 100, 210, 20 for the 215 nm thick film. The pulse and purge times were 0.5/7 s for O_3, 0.5/7.5 s for $Fe(Cp)_2$, and 0.5/7.5 s for $Bi(Ph)_3$, respectively. Using this deposition sequence semi-amorphous superlattices of Fe_2O_3 and Bi_2O_3 were grown with individual growth rates of 0.30 Å/cycle for the ($Fe(Cp)_2$-O_3) subcycle and 0.44 Å/cycle for the ($Bi(Ph)_3$-O_3) subcycle.

XRD measurements were conducted using a Rigaku Smartlab diffractometer equipped with a Cu-source (40kV, 44mA). Lattice parameters were calculated using the WinCSD program package.[44] The cross-sections of 70 nm and 215 nm thick films for transmission electron microscopy (TEM) were prepared using a FEI Strata Dual Beam Focused Ion Beam - Scanning Electron Microscope equipped with an Omniprobe micromanipulator. A standard lift-out procedure was used. TEM experiments were performed on a JEOL JEM2100 operated at 200 keV. Surface morphology and piezoforce response were measured using an Asylum Research MFP-3D atomic force microscope. Note, that for each sample an AC drive voltage of 5 V was used to achieve a stable contact resonance peak before collecting piezoelectric hysteresis loops. The cation ratio was measured on a Zeiss Supra 50VP scanning electron microscope (SEM) equipped with an energy dispersive X-ray spectroscopy (EDS) detector (Oxford Instruments). Precise cation ratio was determined by Rutherford backscattering spectrometry (RBS) for selected films. The backscattered alpha particle spectrometry (BAPS) data were measured utilizing an NEC Pelletron model 5SDH-2 accelerator located at the U.S. Army Research Laboratory, Aberdeen Proving Ground, MD. All measurements were conducted using a 2 MeV He^+ beam with a beam energy spread of ±1.75 keV. The sample beam current was nominally 50 nA and the total integrated beam

current for each sample was about 10 μC. The RBS chamber was operated at a base-pressure of $3x10^{-8}$ Torr. The SIMNRA software package version 6.06 was used to generate RBS simulations and the Rutherford cross sections were utilized in the simulations. X-ray photoelectron spectroscopy (XPS) measurements were conducted using a Physical Electronics VersaProbe 5000 under a base-pressure of $\sim10^{-8}$ Torr. An Al-Kα source provided incident photons with an energy of 1486.6 eV with an irradiation of 10 kW/mm^2.

For electrical measurements, a metal-insulator-metal (MIM) structure according to the schematic in **Figure 1** was used. Top electrodes of 90 x 90 μm^2 in area consisting of 2 nm Cr followed by 50 nm Au were deposited by thermal evaporation after the annealing process. The bottom Pt electrodes were contacted using silver paste. The MIM-structured samples were placed in a probe station (Lakeshore Cryotronics TTP4) and measured in air at room temperature and in vacuum of $\sim10^{-5}$ Torr within the temperature range from -90°C to 150°C utilizing a Model 4200-SCS Semiconductor Characterization System (Keithley Instruments, Inc.). The AC signal output level was set to 30 mV for all electrical measurements. For collecting polarization-electric field hysteresis loops, a Precision Tester (Radiant Technologies, Inc.) was used. The measurements were performed in air at room temperature.

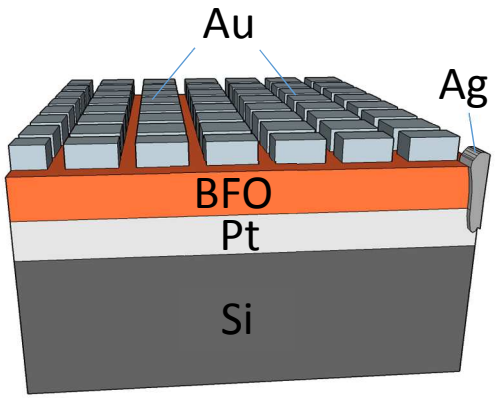

Figure 1. Illustration of the MIM structure used for electrical measurements.

In our previous study we demonstrated that the crystallization behavior of such ALD-deposited BFO films is limited to a rather narrow temperature window between 450°C, where the crystallization sets in, and 600°C, where a substantial evaporation of Bi occurs.[46] Therefore, a post-processing treatment at 550°C was selected for this study.

The different annealing conditions were selected based on numerous studies from literature, which demonstrate that the main sources of conductivity in BFO films are oxygen vacancies and Fe^{2+} ions being formed during the fabrication process.[7-10,47,48] Therefore, annealing in oxygen atmosphere should reduce the number of oxygen vacancies. As nitrogen atmosphere was used by other research groups,[37-40] we decided to include annealing in N_2 for comparison and to better understand the influence of the annealing atmosphere on the resulting properties. It is known that both, intrinsic and extrinsic, *i.e.* native and impurity, defects segregate at grain boundaries. Defects can be the source of increased dielectric losses of the material. Also, point defects located at grain boundaries and the grain boundaries themselves can lead to enhanced electrical conductivity.[49,50] For the beneficial effect of increased grain size and an effective filling of the oxygen vacancies, a prolonged 24 h annealing in O_2 atmosphere was conducted in addition to a short 1 hour annealing duration. Furthermore, a slow cooling to room temperature over a period of 5 h in O_2 (called Ramping herein) was carried out. In total three different annealing durations were applied: 1 h, 24 h and Ramping. For the first two the films were inserted and removed from the furnace at 550°C and air cooled, while for the latter one the heating and cooling was conducted in O_2-flow using a rate of 2 °C/min. Overall, four different annealing procedures were selected: 550°C 1h in N_2, 550°C 1h in O_2, 550°C 24h in O_2, Ramping. Each annealing process was applied to both sets of films.

Results and Discussion

The formation of polycrystalline BFO films without indications for the presence of impurity phases for all samples was confirmed by grazing incidence X-ray diffraction (GI-XRD, see Fig. S1). The lattice parameters (in pseudocubic symmetry) calculated for all films annealed in different conditions are summarized in Table 1, and indicate that the thinner films have smaller lattice parameters than the thicker ones. However, no consistent trend as a function of the annealing conditions is observed.

To get an overview of the morphology across the film and information on the electrode-interface quality, we prepared two samples of different thickness, each annealed for 1 h in N_2, for TEM study. The cross-sections for both films are displayed in **Figure 2**. As expected, the TEM image shows Fe-rich layers for the 70 nm thick film annealed in N_2. These amorphous Fe-rich elongated areas stem from the initial superlattice of alternating FeO_x and BiO_x layers,[46] and extend throughout the cross section of the film. These amorphous layers effectively prevent the BFO grain growth perpendicular to the substrate surface resulting in laterally elongated BFO crystallites confined between the Fe-rich layers. In contrast to this observation, only small, segregated Fe-rich areas are randomly distributed in the stoichiometric 215 nm thick film after annealing in N_2. In both cases the interfaces between the electrodes and film are abrupt and no delamination is observed.

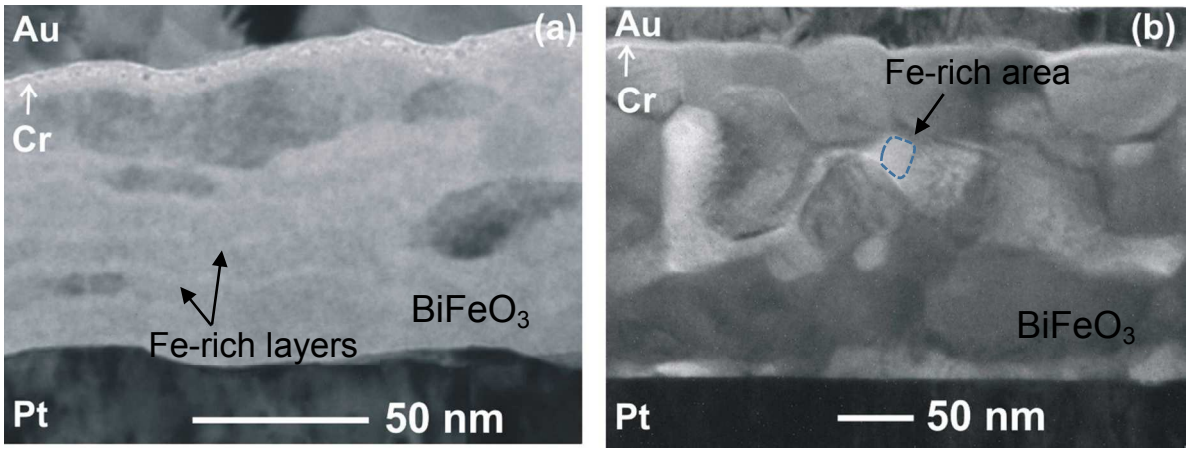

Figure 2. BF-TEM images of the cross-section for 70 nm (a) and 215 nm (b) thick films annealed for 1 h in N_2.

The grain growth and change in surface structure from the as-grown film to the annealed one are illustrated in the AFM images displayed in Fig. S2. The surface roughness and average grain sizes depend strongly on the annealing conditions. As Table 1 shows, the flattest film surface can be obtained after annealing in nitrogen atmosphere, while the roughest film surfaces result from Ramping. The grain sizes are identical after annealing in N_2 and Ramping, and are slightly increased after annealing in O_2. As expected, the largest grain sizes are observed for the films annealed for 24 h in oxygen atmosphere.

Compositional data, namely the Bi/Fe- and O/(Bi+Fe)-ratios are also provided in Table 1, and confirm that the 70 nm thick films are Bi-deficient, while the 215 nm films have a Bi/Fe-ratio close to 1. The annealing conditions have no detectable influence on the Bi/Fe ratio. A detailed evaluation of the RBS results allows understanding how the oxygen content of the thin films depends on the annealing conditions. Compared to annealing in N_2 the O-content is slightly increased in the samples annealed in O_2 atmosphere. This effect is even more pronounced in the thinner Fe-rich films. However, a slow cooling in O_2 atmosphere, as applied for Ramping, surprisingly results in lower oxygen content indicating that this processing method is not suitable for decreasing the amount of oxygen vacancies in BFO thin films. It could be explained as follows. During slow (over 5 hours) cooling bismuth tends to evaporate, and oxygen vacancies appear for charge compensation according to (in Kröger–Vink notation): $2Bi_{Bi}^{x} + 3O_{O}^{x} \leftrightarrow Bi_2O_3(g) + 2\mathrm{v}_{Bi}''' + 3\mathrm{v}_{O}^{\bullet\bullet}$.

Table 1. Lattice parameters from XRD, RMS and grain sizes from AFM (from 5x5 μm^2 area), Bi/Fe ratios from EDS, O/(Bi+Fe) from RBS and Fe^{2+}/Fe^{3+} from XPS for the 70 nm and 215 nm thick films, annealed at different conditions

Parameter	550°C 1h in N_2		550°C 1h in O_2		550°C 24h in O_2		Ramping	
	70-nm	215-nm	70-nm	215-nm	70-nm	215-nm	70-nm	215-nm
Lattice parameter (in Å)	3.952(6)	3.947(4)	3.957(4)	3.949(3)	3.965(6)	3.943(4)	3.952(3)	3.939(4)
RMS roughness (in nm)	6.4	10.9	9.0	9.1	7.2	15.3	11.0	18.0

Average grain sizes (in nm)	93	95	137	106	226	142	90	98
Bi/Fe	0.6	1.1	0.7	0.9	0.6	1.0	0.6	1.0
O/(Bi+Fe)[1]	1.516	1.791	1.814	1.837	-	-	1.604	1.682
Fe^{2+}/Fe^{3+}	-	0.35	0.09	-	-	-	0.09	0.09

[1]RBS data obtained for samples deposited on Si substrates.

In order to gain information on the Fe^{2+} content of these thin films, we conducted XPS measurements. The fittings of the spectra reveal that for the 215-nm films, the Fe^{2+}/Fe^{3+} ratio is 0.35 after annealing for 1h in N_2 (Fig.3a) and decreases to 0.09 after Ramping (Fig.3b), demonstrating that annealing in oxygen atmosphere is an effective method to sustain most of Fe-species in the 3+-oxidation state. Consistent with this observation for the 70 nm thick films, the Fe^{2+}/Fe^{3+} ratio is 0.09 after both annealing procedures, for 1 h in O_2 and Ramping (see Fig.S3). Comparing these results with the O/(Bi+Fe) ratios, all shown in Table 1, we find that for the 70-nm Fe-rich films the O/(Bi+Fe) ratio is higher by a factor of 1.13 after annealing for 1 h in O_2 compared to the Ramping procedure. This indicates that the amount of oxygen vacancies is higher after Ramping. As the Fe^{2+}/Fe^{3+} ratio is similar for both samples and assuming overall charge neutrality, these additional oxygen vacancies are correlated to the presence of bismuth vacancies, which form during the Ramping treatment, where an enhanced loss of Bi close to the film surface could arise. For the 215-nm films, the O/(Bi+Fe) ratio remains almost unchanged between annealing in N_2 and Ramping, while the Fe^{2+}/Fe^{3+} ratio drops dramatically by a factor of 3.9 insinuating that the film after Ramping should be less conductive. Indeed, this expectation is confirmed by the electrical measurements (see Fig.5).

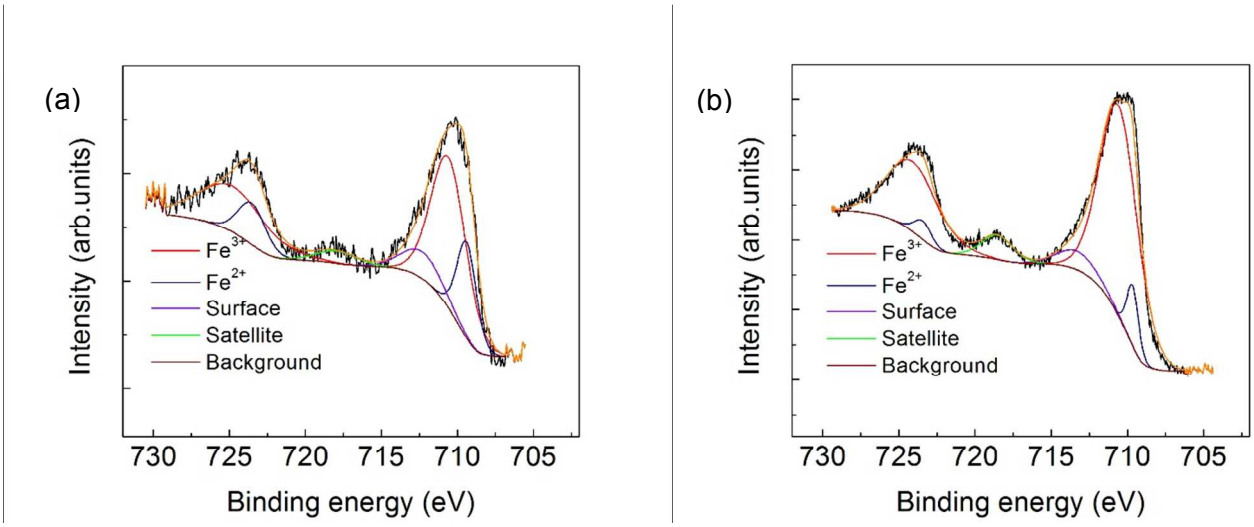

Figure 3. Fitting of the experimental XPS iron spectra collected for the 215-nm stoichiometric film annealed: (a) for 1h in N_2 and (b) under Ramping.

To locally probe the ferroelectric switching and potential influences of the annealing conditions on the piezoelectric response, PFM measurements on two 70 nm thick films were conducted. Representative piezoelectric hysteresis loops for the amplitude and phase are displayed in **Figure 4** for the 70 nm thick films annealed for 1 h in N_2 and O_2. Interestingly, the piezoelectric response is qualitatively very similar in amplitude as well as phase for both films. This observation demonstrates that the piezoelectric properties of grains at the surface are insensitive to the annealing atmosphere. The ability to orient and reorient domains using PFM is shown in Fig.S4. The macroscopic ferroelectricity of the thin films was probed by collecting polarization-electric field (P-E) hysteresis loops at room temperature. The P-E loops for two representative 215 nm thick films annealed for 1 h and 24 h in O_2 are displayed in Fig. S5. While the total polarization obviously caused by leakage current decreases, the remnant polarization increases from 0.12 $\mu C/cm^2$ for the sample annealed for 1 h in O_2 to 0.20 $\mu C/cm^2$ for the sample annealed for 24 h in O_2. Note that we obtained a non-saturated P-E loop due to the electrical breakdown. Also a non-saturated P-E dependence with remnant polarization varying from 1 to 5 $\mu C/cm^2$ was registered by Puttaswamy *et al.*[42] on 200 nm thick ALD-grown BFO thin films. The non-

saturated P-E loops with relatively low remnant polarization observed in polycrystalline films can be attributed to the random orientation of grains throughout the film. At the same time a well saturated hysteretic response for the PFM measurements shows clear evidence for the ferroelectricity of individual grains.

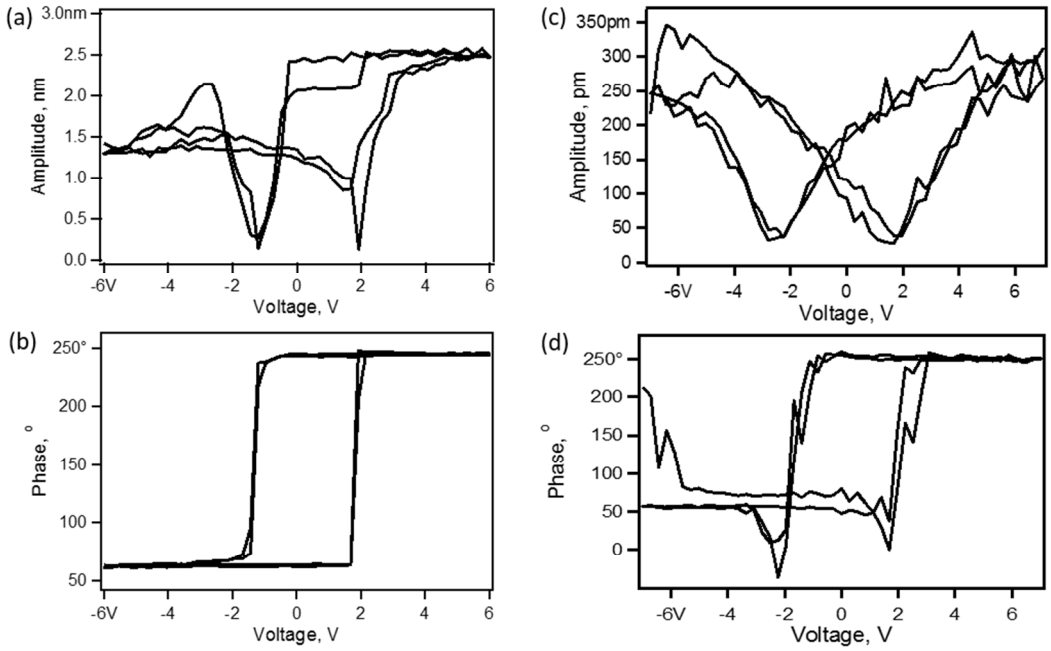

Figure 4. Hysteretic behavior of piezoelectric amplitude (a, c) and phase (b, d) in the 70 nm thick film annealed for 1 h in O_2 (a, b) and N_2 (c, d) measured by PFM.

Comparing the influence of annealing conditions on the current density for the two film sets (**Figure 5)** shows that the Fe-rich films are in general leakier than the stoichiometric ones, and that the annealing conditions have a much stronger effect on the leakage current in the Fe-rich films. While the current density is an order of magnitude lower after annealing in N_2 than after annealing in O_2 in a thinner Fe-rich film, the current is only slightly lower after annealing in N_2 compared with O_2 in a thicker stoichiometric film. Still, the tendency of a decreased leakage current for annealing in N_2 is observed for both film thicknesses. The lowest leakage currents are observed after 24 h annealing in O_2

for the thinner films and after Ramping for the thicker films. Taking the RBS and XPS data presented above into account, which indicate that there are less oxygen vacancies and Fe^{2+} ions after annealing in O_2 than in N_2, we can explain this effect of substantial leakage current reduction after annealing in N_2 in the Fe-rich film as follows: we assume that oxygen vacancies are the dominating source for leakage resulting in n-type conductivity, which was confirmed for epitaxial PLD grown BFO films.[25] The formation mechanism of O-vacancies results most likely from the low temperature deposition and can be described as: $O_O^x \leftrightarrow \frac{1}{2}O_2(g) + 2e' + \mathrm{v}_O^{\bullet\bullet}$. During the N_2 annealing the recharging of Fe^{3+} to Fe^{2+} is promoted: $Fe_{Fe}^x + e' \leftrightarrow Fe_{Fe}'$. This recharging process lowers the number of electrons, hence, decreases the leakage current. While annealing in O_2 for only 1h appears to be insufficient to effectively fill the oxygen vacancies, extensive annealing periods result in a compensation, which has a stronger effect and ultimately reduces the leakage current. Also more complex scenarios have to be considered: first, at higher concentrations cation and anion defects could compensate each other and therefore reduce the free charge carrier density as was suggested by the authors of Ref. [25] for epitaxial BFO films. Furthermore, interface phenomena, particularly at the interfaces between neighboring grains, *i.e.*, grain boundaries, are expected to remarkably contribute to the conductivity in our films. It was shown that in polycrystalline films, compared to epitaxial ones, grain boundaries serve as additional conduction pathways, for example, due to segregation of oxygen vacancies and charge accumulation at the grain boundaries.[49,50] In such a case, the higher amount of oxygen vacancies in the film annealed in N_2 located at the grain boundaries could contribute less to the conductivity, in agreement with the smaller average grain size and therefore the overall larger length of grain boundaries compared to the film annealed in O_2 (see Table 1).

With respect to the size effect, in particular for the influence of the film thickness on the leakage current, contradicting data exist in the literature. While other reports demonstrate that leakage current is

higher for thinner films,[51,52] Marchand *et al.*[40] show a substantial decrease of the leakage current with decreasing film thickness; it reduces by 2 orders of magnitude as the thickness decreases from 500 nm to 200 nm and by an additional 2 orders of magnitude for the 50 nm thick films. The authors explain this decrease by the overall strain, which causes a more prominent distortion over the film depth, including hillocks, and partial delamination resulting in more conductive interfaces and paths through the film in the thicker films compared to the thinner ones. As shown in Fig. 2, there is no delamination in both, 70 nm and 215 nm thick films. Therefore, in the present case, the leakage current increases in the thinner films. One factor, which would promote this increase, is a dominant contribution of the interface-limited Schottky emission for thinner films. Indeed, this is corroborated by the fitting results presented below.

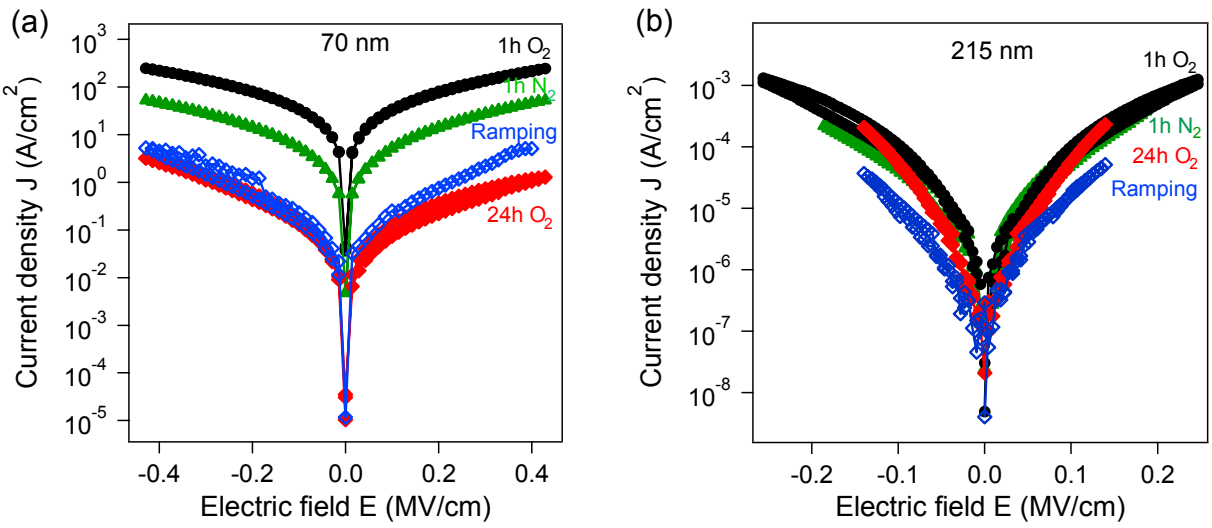

Figure 5. Room-temperature electric-field dependences of current density for the 70-nm Fe-rich (a) and the 215-nm stoichiometric (b) films annealed under different annealing conditions.

To gain a deeper insight into the nature of conductivity, different conduction mechanisms can be considered. Because the electric-field dependences are symmetric in positive and negative bias directions, the analysis was conducted for the positive upward bias for all samples. We consider Schottky emission, Poole-Frenkel (PF) emission and space-charge-limited conduction (SCLC)

mechanisms, which are commonly observed in perovskite oxides, and particularly in BFO films.[53-55] The relation between current density, J (or conductivity σ), and voltage, V, for each of these mechanisms is provided:

Schottky emission: $J_S = AT^2 exp - [\frac{\Phi}{k_B T} - \frac{1}{k_B T}\sqrt{\frac{q^3 V}{4\pi\varepsilon_0 K d}}]$ (1)

Poole-Frenkel emission: $\sigma_{PF} = c\ exp - \left[\frac{E_I}{k_B T} - \frac{1}{k_B T}\sqrt{\left(\frac{q^3 V}{\pi\varepsilon_0 K d}\right)}\right]$ (2)

SCLC mechanism: $J_{Ohm} = \frac{q n_0 \mu V}{d}$, $J_{TFL} = \frac{9}{8}\mu\varepsilon\Theta\frac{V^2}{d^3}$, $J_{Child} = \frac{9}{8}\mu\varepsilon\frac{V^2}{d^3}$ (3)

In equations (1)-(3), A is the Richardson constant, T is the temperature, Φ is the height of the Schottky barrier, k_B is the Boltzmann constant, q is the elementary charge, V is the applied voltage, ε_0 is the permittivity of free space, K is the optical dielectric constant, d is the sample thickness, c is a constant, E_I is the trap ionization energy, n_0 is the concentration of the free charge carriers in thermal equilibrium, μ is the mobility of charge carriers, ε is the static dielectric constant and Θ is the ratio of the free carrier density to total carrier (free and trapped) density.

As equations (1) and (2) show, Schottky and Poole-Frenkel emission are similar in terms of current-voltage relationship, but the first one is interface-limited, while the second one is bulk-limited. Representative dependences for these different mechanisms are shown in **Figure 6**. For clarity, we omitted plotting the data for the 215 nm thick sample annealed in N_2, as it practically follows the one annealed for 1h in O_2.

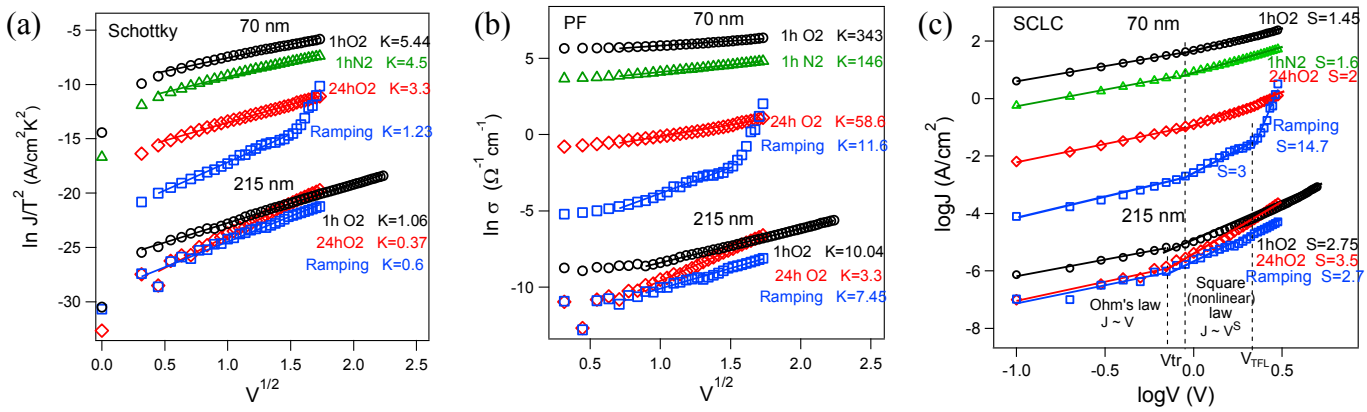

Figure 6. Fitting results for the experimental data considering different conduction mechanisms: Schottky emission (a), Poole-Frenkel (PF) emission (b) and SCLC mechanism (c).

In general, each mechanism contributes to the electrical conductivity, so strictly speaking, we can identify only the dominating mechanism. As the slopes of the curves for the Schottky emission and Poole-Frenkel emission are correlated to the optical dielectric constant *K*, the dominating mechanism should give a value close to the optical dielectric constant of the material. The values of *K* calculated from the slopes of the curves are provided in Figs. 6a and 6b. As the optical dielectric constant for BFO is 6.25,[56] we can determine that the interface-limited Schottky mechanism mainly contributes to the current density in the 70 nm thick films, although the contribution is reduced as the leakage current decreases for the different annealing conditions. The bulk-limited Poole-Frenkel mechanism has a stronger contribution to the leakage current in the 215 nm thick films, while for the thinner films unreasonable values for K exclude this mechanism. These results can be understood considering that the ratio between the interface layer (near-electrode defective area) and bulk is much smaller for the thicker films compared to the thinner ones. The space-charge-limited conduction mechanismis usually analyzed by evaluating the voltage dependence of the current density in double-logarithmic plots. It should be noted, that in some papers on BFO, a SCLC mechanism is ruled out because the experimental data are fitted only to Child's law (see equations (3)), while the log*J*-log*V* dependence is actually comprised of

three distinct regions, namely, Ohm's law, traps-filled limit (TFL) current, and Child's law with the points V_{tran} and V_{TFL} which are the transition voltages between the regions.[57,58] Out of these three regions for the SCLC mechanism we can identify two regions in our films, Ohm's and traps-filled ones for most of our samples, but not Child's law behavior at the highest fields because of the occurrence of dielectric breakdown before that. The third region has been registered only in the 70 nm thick film annealed in the Ramping procedure. In all 70-nm films, the transition voltage V_{tran} is 0.9 V, corresponding to an electric field E_{tran}=128 kV/cm, while for the 215 nm samples V_{tran} is 0.7 V corresponding to E_{tran} = 40 kV/cm. Note that V_{tran} is the voltage at which the transition from Ohm's law to SCLC takes place. At this point, the traps are filled up and a space charge appears. Therefore, the higher value of V_{tran} in the 70-nm films compared with the 215-nm films points towards a higher amount of traps in the Fe-rich films. As shown in Table 1, in these films the oxygen content is lower, which means that the amount of oxygen vacancies is higher than in the stoichiometric 215-nm films. Based on this observation, we can state that the oxygen vacancies play the role of trap centers in our films. Figure 6c shows that a pure square region when $S = 2$ in the relation $J \sim V^S$, occurs in the thinner film after annealing for 24 h in O_2, while $S < 2$ for the samples annealed for 1 h in O_2 and N_2, and $S > 2$ for the sample annealed under Ramping procedure as well as for all 215 nm thick samples. As mentioned in Refs. [59] and [60], a pure square region rarely occurs, and a nonlinear region ($S > 2$) is observed in solids instead. Overall, the Schottky emission mechanism is dominant in the thinner films after annealing for 1 h in O_2 and N_2, while an SCLC conduction mechanism is dominant in the 70 nm thick films annealed for 24 h in O_2 and under Ramping procedure as well as in all 215 nm thick films independent of the annealing conditions. Additionally, Poole-Frenkel emission contributes in the 215 nm thick film after Ramping. Note that both, Poole-Frenkel and SCLC mechanisms occur due to the presence of trap levels E_{tr} being created in the band gap of the BFO film.

To determine the trap energy level E_{tr}, the influence of the temperature on the leakage current has been investigated. It was found that leakage current increases slightly with temperature in the 70 nm thick films, while it increases significantly at elevated temperatures in the 215 nm thick film. **Figure 7a** shows the electric-field dependences of the current density at representative temperatures obtained for the 215 nm thick film annealed for 24 h in O_2. Note, that the observed hysteresis in current is considered as a unipolar resistive switching, as it allows to switch the film between high-resistance state (HRS) and low-resistance state (LRS) at one voltage polarity.[61] Filamentary formation and oxygen vacancy migration are typical microscopic origins for this phenomenon.[61,62] The hysteresis in current is much lower for the thinner 70 nm films. Such a thickness-dependent resistive switching was observed by A. Rana et al.[63] The resistive switching is barely dependent on annealing conditions. **Figure 7b** shows that the temperature dependence of the conductivity follows an Arrhenius behavior, i.e. $\sigma = \sigma_0 \exp(-E_a/kT)$, where σ_0 is the pre-exponential factor and E_a is the activation energy. Generally speaking, the activation energy corresponds to the energy gap between the Fermi level E_F and the bottom of the conduction band E_c of the material (inset in Fig. 7b). In the case of BFO, the defects form the trap level E_{tr} in band gap. Therefore, the activation energy E_a is actually the gap between the trap level E_{tr} and conduction band E_c. The value E_a = 0.66 eV is obtained from the temperature dependence of the conductivity shown in Fig. 7b. Taking into account that the band gap in BFO is about 2.5-2.8 eV,[64] the trap level E_{tr} lies higher than the Fermi level E_F as illustrated in the schematic energy levels presented in Fig. 7b.

Also, the role of the grain boundaries and their effect on the leakage current in polycrystalline BFO films should be mentioned: on one hand, we observe reduced leakage current with increasing grain sizes after certain annealing procedures, on the other hand, taking into account the TEM data, we should note that Fe-rich areas, which align mostly along the grain boundaries in the thinner film, are expected

to contribute to the conductivity of the material reducing the current, while the isolated spherically-shaped Fe-rich areas present in the thicker film do not influence the leakage current.

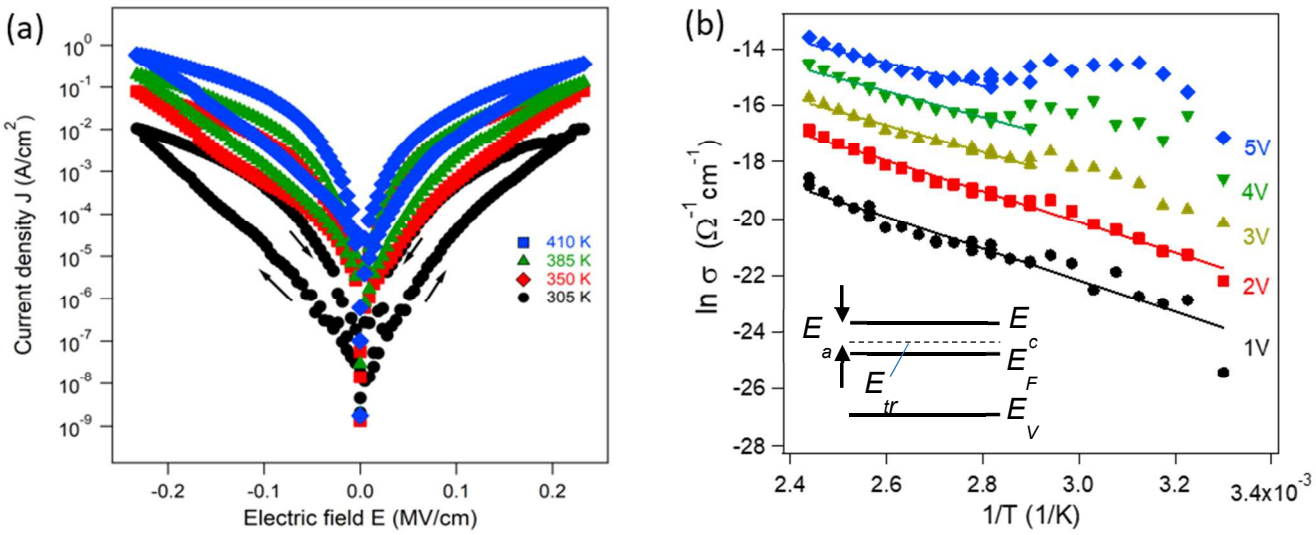

Figure 7. Electric-field dependence of the current density at different temperatures (a) and logarithmic representation of the conductivity versus temperature (b) for a 215 nm thick film annealed for 24 h in O_2.

Interestingly, annealing in oxygen atmosphere decreases drastically the low-frequency (~10^4 Hz) dielectric losses and has a smaller effect on high-frequency (~10^6 Hz) losses in the thinner films (Fig.8a), while the dielectric losses for the thicker films are only moderately and equally affected in the entire frequency range (Fig.8b). Usually, low-frequency losses are due to the reorientation of space charges, which are formed in the near-electrode layer or at the interface between electrode and film. Therefore, this observation is consistent with our analysis of the conduction mechanisms, and confirms that the contribution of contact interface phenomena to the leakage current is more pronounced in the thinner films. Since oxygen vacancies can be the origin of both, space charges and dipole centers, evidently the prolonged annealing in O_2 and Ramping decrease the amount of oxygen vacancies. Further analyzing frequency dependence of dielectric losses, we should notice that in a case the relaxation

phenomena take place in the material, frequency dependence for the real and imaginary components of the dielectric permittivity in polar dielectric materials is described by the Debye[65] or the Cole-Cole[66] model. If relaxation processes occur, they manifest themselves by the maximum in the temperature dependence of dielectric loss. However, we do not observe any maxima in the frequency dependences of dielectric losses within the temperature range from -90^{0}C to 150^{0}C in our samples. This result indicates that oxygen vacancies act as trap centers for the charge carriers (electrons) rather than contribute to the reorientation of the dipole centers in the material. Note, that activation energies in the range of 0.6–1.2 eV are associated with doubly-ionized oxygen vacancies for perovskite-type ferroelectrics.[67] Thus, it can be concluded that dielectric losses in these films are more of conductive than relaxation nature. This implies that dielectric losses should be further decreased at frequencies above 1 MHz.

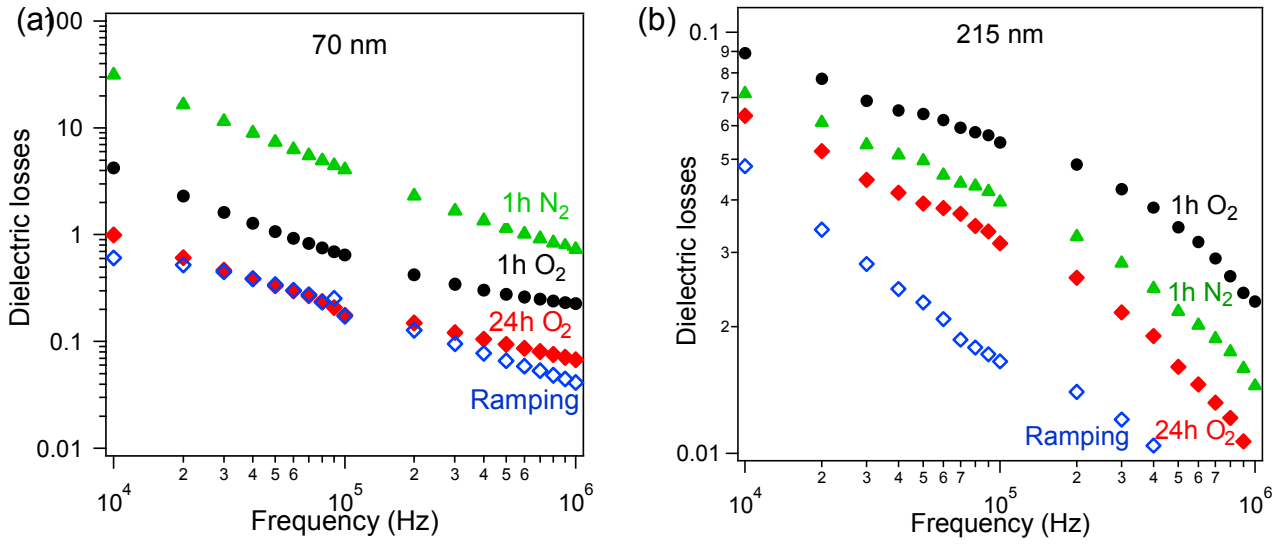

Figure 8. Frequency dependences of dielectric losses for 70 nm (a) and 215 nm (b) thick films after different annealing procedures

Decreasing the leakage current after certain annealing procedures results in a reduction of the dielectric constant in the 70 nm thick films (Fig.9a). This observation could be interpreted as evidence

that space charges accumulated at the grain boundaries and film-electrode interfaces act as the main contributor to enhanced dielectric permittivity in 70 nm thick films.[2] The annealing conditions affect the dielectric constant differently in the 215 nm thick films (Fig.9b). While the leakage current and losses decrease after annealing for 24 h in O_2 and Ramping for the thinner films, the dielectric constant remains unchanged in the thicker films. Contrarily, the current and losses are higher after annealing for 1 h in O_2 and N_2, but the dielectric constant is lower after these annealing procedures in the thicker films. Such a behavior could also result from the influence of grain boundaries.

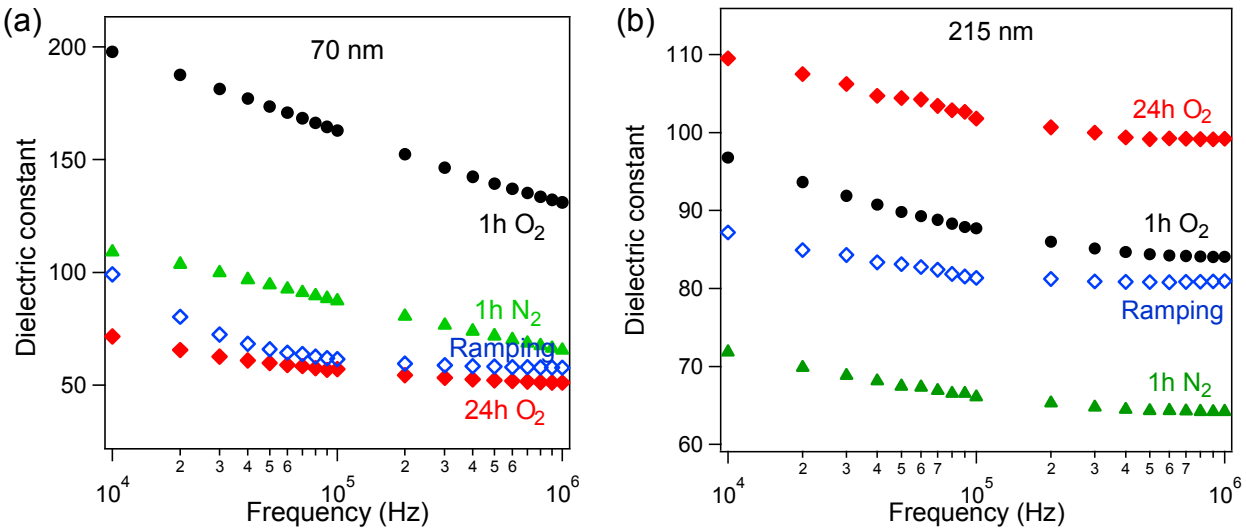

Figure 9. Frequency dependences of the dielectric constants for the 70 nm (a) and the 215 nm (b) thick films after different annealing procedures.

A low dielectric constant is detrimental in terms of tunability, as the tunability generally decreases with decreasing dielectric constant (see **Fig. 10a**). The dielectric losses remain almost unchanged under bias field for the films as shown in **Fig. 10b**. In addition, **Figure 10c** shows that tunability increases with increasing frequency for the 70 nm thick film annealed for 1h in O_2.

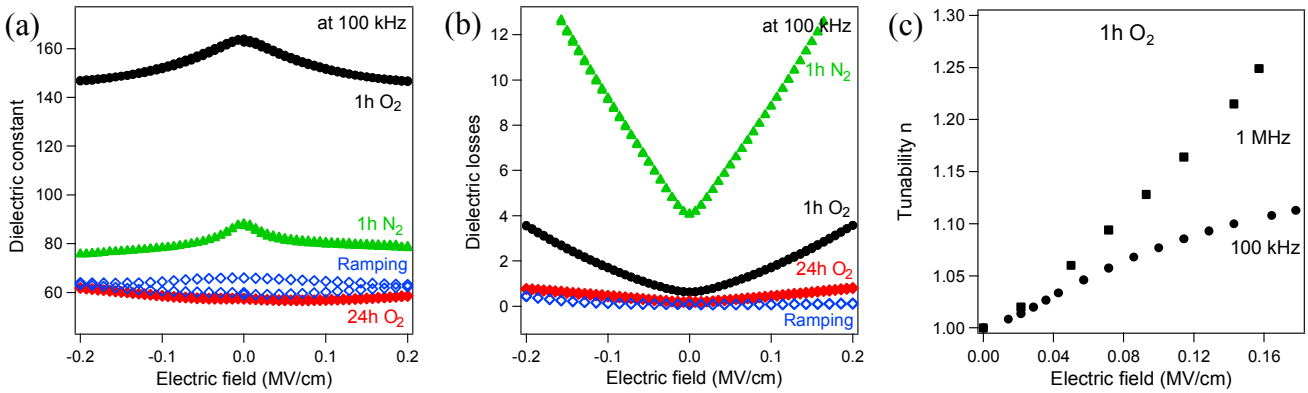

Figure 10. Electric-field dependences of the dielectric constant (a) and the dielectric losses (b) versus annealing procedure for the 70 nm thick films at 100 kHz, and of the tunability at 100 kHz and 1 MHz (c) for the film annealed for 1h in O_2.

These controversial tendencies indicate that for specific application and relevant functional requirements there are annealing conditions, which can provide an optimal trade-off between such parameters as leakage current, losses and dielectric constant to provide high performance of the material.

Conclusion

In summary, we investigated the influence of different annealing procedures on the conductivity and dielectric properties of 70 nm thick Fe-rich and 215 nm thick stoichiometric BFO films. It was found that a bulk-limited SCLC mechanism is dominant in the thicker films, while a contribution of the interface-limited Schottky emission is more prominent in the thinner films. Analysis reveals that prolonged annealing in oxygen atmosphere promotes grain growth by a factor of 2.5, and therefore reduces defect density at the grain boundaries. In turn, this grain growth leads to a reduction in leakage current by 2 orders of magnitude in the thinner films. After prolonged annealing in O_2, the losses become lower, while the dielectric constant remains high in the thicker films. In contrast to this observation, the increased dielectric constant and losses for the thinner films are clearly correlated to the higher leakage current, which both are decreased after excessive annealing in O_2 atmosphere. In general, our results highlight that a proper selection of annealing conditions is crucial for optimizing the

properties of BFO thin films for a particular application, e.g. improved electrical characteristics such as a 100-fold reduction in leakage current and a 10-fold decrease in low-frequency losses have been obtained after extensive annealing for the thinner films.

Conflicts of interest

There are no conflicts to declare.

Acknowledgments

Work at Drexel University was supported by the Office of Naval Research under grant N00014-15-11-2170. The research was partially sponsored by the Army Research Laboratory and was accomplished under Cooperative Agreement No. W911NF-12-2-0019. The authors also acknowledge the Drexel core shared facilities and NSF DMR 1040166 and NSF CBET 0959361.

References

1 W. Eerenstein, N. D. Mathur and J. F. Scott, *Nature,* 2006, **442**, 759-765.

2 G. Catalan, and J. F. Scott, *Adv. Mater.*, 2009, **21**, 2463–2485.

3 H. Béa, M. Gajek, M. Bibes, and A. Barthélémy, *J. Phys.: Condens. Matter*., 2008, **20**, 434221.

4 S. Fujino, M. Murakami, V. Anbusathaiah, S.-H. Lim, V. Nagarajan, C. J. Fennie, M. Wuttig, L. Salamanca-Riba and I. Takeuchi, *Appl. Phys. Lett*., 2008, **92**, 202904.

5 K. Takahashi, N. Kida and M. T. Tonouchi, *Phys. Rev. Lett*., 2006, **96**, 117402.

6 V. Ryzhii, *J. Phys.: Condens. Matter,* 2008, **20**, 380301.

7 W. Eerenstein, F. D. Morrison, J. Dho, M. G. Blamire, J. F. Scott and N. D. Mathur, *Science,* 2005, **307**, 1203a.

8 J. Dho, X. Qi, H. Kim, J. L. MacManus-Driscoll and M. G. Blamire, *Adv. Mater*., 2006, **18**, 1445-1448.

9 V. R. Palkar, J. John and R. Pinto, *Appl. Phys. Lett.,* 2002, **80**, 1628-1630.

10 T. Ito, T. Ushiyama, M. Aoki, Y. Tomioka, Y. Hakuta, H. Takashima and R. Wang, *Inorg. Chem.,* 2013, **52**, 12806-10.

11 H. Béa, M. Bibes, A. Barthélémy, K. Bouzehouane, E. Jacquet, A. Khodan, J.-P. Contour, S. Fusil, F. Wyczisk, A. Forget, D. Lebeugle, D. Colson and M. Viret, *Appl. Phys. Lett.,* 2005, **87**, 072508.

12 Z. V. Gabbasova, M. D. Kuz'min, A. K. Zvezdin, I. S. Dubenko, V. A. Murashov, D. N. Rakov and I.B. Krynetsky, *Phys. Lett. A,* 1991, **158**, 491-498.

13 Y. Qi, B. Alima and Z. Shifeng, *Journal of Rare Earths,* 2014, **32**, 884-889.

14 Z.-L.Hou, H.-F. Zhou, L.-B. Kong, H.-B. Jin, X. Qi and M.-S. Cao, *Materials Letters,* 2012, **84**, 110–113.

15 L. Jin, W. B. Luo, X. Qing, Y. Shuai, C. Yang, C. G. Wu and W. L. Zhang, *Materials Research Innovations,* 2015, **19**, S7-35.

16 G. S.Lotey and N. K. Verma, N. K., *J Nanopart Res,* 2012, **14**, 742.

17 G. S. Lotey and N. K. Verma, *Chemical Physics Letters,* 2013*,* **574**, 71–77.

18 C. Nayek, Ch.Thirmal, A. Pal and P. Murugavel, *Materials Science and Engineering: B,* 2015, **199**, 121–124.

19 M. A. Basith, O. Kurni, M. S. Alam, B. L. Sinha and B. Ahmmad, *Journal of Appl. Physics,* 2014, **115**, 024102.

20 M.S.B. Darby, D.V. Karpinsky, J. Pokorny, S. Guerin, A.L. Kholkin, S. Miao, B.E. Hayden, and I.M. Reaney, *Thin Solid Films*, 2013, **531**, 56-60.

21 D. Arnold, .*IEEE Transactions on Ultrasonics, Ferroelectrics, and Frequency Control,* 2015, **62**, 62-82.

22 H. W. Chang, F. T. Yuan, S. H. Tien, P. Y. Li, C. R. Wang, C. S. Tu and S. U. Jen, *Journal of Appl. Physics,* 2013, **113**, 17D917.

23 M. Yi, C. Wang, Q. Shen and L. Zhang, *Advanced Materials Research,* 2013, **760-762**, 714-718.

24 J. M. Park, S. Nakashima, M. Sohgawa, T. Kanashima and M. Okuyama, *Ferroelectrics,* 2013, **453**, 1–7.

25 L. R. Dedon, S. Saremi, Z. Chen, A. R Damodaran, B. A. Apgar, R. Gao and L. W. Martin, Chem. Mater., **2016**, ***28*** (16), 5952–5961.

26 F. Fan, B. Luo, M. Duan and C. Chen, *Journal of Applied Spectroscopy,* 2013, **80**, 378-383.

27 G. Drera, A. Giampietri, I. Alessandri, E. Magnano, F. Bondino and S. Nappini, *Thin Solid Films* 2015, **589**, 551–555.

28 S. K. Chang and Y.-J. Kim, Journal of the Korean Physical Society, 2014, **65**, 1063-1067.

29 L. Jin, X. Tang, D. Song, R. Wei, J. Y. J. Dai, W. Song, X. Zhu and Y. Sun, J. *Mater. Chem. C,* 2015, **3**, 10742.

30 J. F. Ihlefeld, D. T. Harris, R. Keech, J. L. Jones, J.-P. Maria and S. Trolier-McKinstry, J. *Am. Ceram. Soc.,* 2016, **99**, 2537–2557.

31 K. Kaemmer, H. Huelz, B. Holzapfel, W Haessler and L. Schultz, *J. Phys. D: Appl. Phys.,* 1997, **30**, 522–526.

32 M. George, *Chem. Rev.* 2010, **110**, 111–131.

33 V. Miikkulainen, M. Leskela, M. Ritala and R. L. Puurunen, R. L. Crystallinity of inorganic films grown by atomic layer deposition: Overview and general trends. J. Appl. Phys. 2013, **113**, 021301.

34 J. S.Ponraj, I. G. Attolin and M Bosi, *Solid State Mater. Sci*., 2013, **38**, 203–233.

35 A. R. Akbashev, G. Chen and J. E. Spanier, *Nano Lett.,* 2013, **14**, 44−49.

36 F. Zhang, G. Sun, W. Zhao, L. Wang, L. Zheng, S. Liu, B. Liu, L. Dong, X. Liu, G. Yan, L. Tian and Y. Zeng, *J. Phys. Chem. C,* 2013, **117**, 24579−24585.

37 A. R. Akbashev, A. V. Plokhikh, D. Barbash, S. E. Lofland and J. E.; Spanier, J.E., *APL Materials,* 2015, **3**, 106102.

38 M. Coll, J. Gazquez, I. Fina, Z. Khayat, A. Quindeau, M. Alexe, M. Varela, S. Trolier-McKinstry, X. Obradors and T. Puig, *Chem. Mater.,* 2015, **27**, 6322−6328

39 C. D. Pham, J. Chang, M. A. Zurbuchen and J. P. Chang, *Chem. Mater*., 2015, **27**, 7282−7288.

40 B. Marchand, P. Jalkanen, V. Tuboltsev, M. Vehkamäki, M. Puttaswamy, M. Kemell, K. Mizohata, T. Hatanpa, A. Savin, J. Räisänen, M. Ritala and M. Leskela, *J. Phys. Chem. C,* 2016, **120**, 7313−7322.

41 P. Jalkanen, V. Tuboltsev, B. Marchand, A. Savin, M. Puttaswamy, M. Vehkamäki, K. Mizohata, M.; Kemell, T. Hatanpää, V. Rogozin, J. Räisänen, M Ritala and M. Leskelä, *J. Phys. Chem. Lett.,* 2014, **5**, 4319−4323.

42 M. Puttaswamy, M. Vehkamäki, K. Kukli, M. C. Dimri, M. Kemell, T. Hatanpää, M. J. Heikkilä, K. Mizohata, R. Stern, M. Ritala and M. Leskelä, *Thin Solid Films* 2016, **611**, 78–87.

43 A. Lahma, K. Zhao, S. Habouti, M. Dietze, C.-H. Solterbeck and M. Es-Souni, *Solid State Ionic,* 2011, **202**, 1–5.

44 S. Fujino, M. Murakami, S.-H. Lim, M. Wuttig, L. G. Salamanca-Riba and I. Takeuchi, *Solid State Ionics,* 2007, **178**, 1257.

45 L. Akselrud, and Y. Grin, *J. Appl. Cryst.,* 2014, **47**, 803-805.

46 A. V. Plokhikh, M. Falmbigl, I. S. Golovina, A. R. Akbashev, I. A. Karateev, M. Y. Presnyakov, A. L. Vasiliev and J. E. Spanier, *ChemPhysChem,* 2017*,* **18**, 1966-1970.

47 H.Yang, Y. Q. Wang, H. Wang and Q. X. Jia, *Appl. Phys. Lett.,* 2010, **96**, 012909.

48 W. B. Luo, J. Zhu, Y. R. Li, X. P. Wang, D. Zhao, J.Xiong and Y. Zhang, *Appl. Phys. Lett*., 2007, **91**, 082501.

49 K. Yin, M. Li, Y. Liu, C. He. F. Zhuge, B. Chen, W. Lu, X. Pan and R. Li., *Appl. Phys. Lett.,* 2010, **97**, 042101.

50 B. Stojadinovic, B. Vasic, D. Stepanenko, N. Tadic, R. Gajic and Z. Dohcevic-Mitrovic, *J. Phys. D: Appl. Phys,.* 2016, **49**, 045309.

51 Xianwu Tang, Jianming Dai, Xuebin Zhu, Jianchao Lin, Qing Chang, Dajun Wu, Wenhai Song, and Yuping Sun, *J Am Ceram Soc* 2012, **95**, 538–544.

52 H. I. Choi, S. W. Kim, J. W. Kim, D. Do, S. S. Kim and W. J. Kim, M. H. Lee, J. S. Park, H. J. Cho, D. J. Kim, J. H. Cho and T. K. Song, *Journal of the Korean Physical Society* 2012, **60**, 288-291.

53 G. W. Pabst, L. W. Martin, Y.-H. Chu, R. Ramesh, *Appl. Phys. Lett*., 2007, **90**, 072902.

54 H. Yang, M. Jain, N. A. Suvorova, H. Zhou, H. M. Luo, D. M. Feldmann, P. C. Dowden, R. F. DePaula, S. R. Foltyn and Q.X. Jia, *Appl. Phys. Lett*., 2007, **91**, 072911.

55 S. Nakashima, T. Ito, H. Fujisawa, T. Kanashima, M. Okuyama, M. Kobune and M. Shimizu, *Jpn. J. Appl. Phys*., 2014, **53**, 08NA01.

56 S. Iakovlev, C.-H. Solterbeck, M. Kuhnke and M. Es-Souni, *J. Appl.Phys.*, 2005, **97**, 094901.

57 K.-C. Kao and W. Hwang, *Electrical Transport in Solids with Particular Reference to Organic Semiconductors;* Pergamon Press, Oxford, 1981.

58 S. M. Sze and K. K. Ng, *Physics of Semiconductor Devices;* Wiley-Interscience: Hoboken, 2007.

59 H. Matsuo, Y. Kitanaka, R. Inoue, Y. Noguchi and M. Miyayama, *J. Appl. Phys.,* 2015*,* **118**, 114101.

60 D. Lee, S. H. Baek, T. H. Kim, J.-G. Yoon, C. M. Folkman, C. B. Eom and T. W. Noh, *Phys. Rev. B*, 2011, **84**, 125305.

61 R. Waser, R. Dittmann, G. Staikov, and K. Szot, *Adv. Mater*. 2009, **21**, 2632–2663.

62 K. Yin, M. Li, Y. Liu, C. He, F. Zhuge, B. Chen, W. Lu, X. Pan, and R.-W. Li, *Appl. Phys. Lett.* 2010, **97**, 042101.

63 A. Rana , H. Lu , K. Bogle , Q. Zhang , R. Vasudevan, V. Thakare , A. Gruverman , S. Ogale, and N. Valanoor, *Adv. Funct. Mater*. **2014**, 24, 3962–3969.

64 S. J. Clark and J. Robertson, *Appl. Phys. Lett.*, 2007, **90**, 132903.

65 P. Debye, *Polar Molecules*, Chemical Catalogue Company, New York, 1929.

66 K. S. Cole and R. H.Cole, *J. Chem. Phys.*, 1941, **9**, 341-351.

67 D. M. Smyth, *Journal of Electroceramics*, 2003**, 11**, 89-100.

We show that a proper selection of annealing conditions is crucial for optimizing the properties of ALD-grown $BiFeO_3$ thin films.